

Daytime O/N₂ Retrieval Algorithm for the Ionospheric Connection Explorer (ICON)

Andrew W. Stephan¹ · R.R. Meier^{2,3} · Scott L. England⁴ ·
Stephen B. Mende⁵ · Harald U. Frey⁵ ·
Thomas J. Immel⁵

Received: 25 August 2017 / Accepted: 23 January 2018 / Published online: 30 January 2018
© This is a U.S. Government work and not under copyright protection in the US; foreign copyright protection may apply 2018

Abstract The NASA Ionospheric Connection Explorer Far-Ultraviolet spectrometer, ICON FUV, will measure altitude profiles of the daytime far-ultraviolet (FUV) OI 135.6 nm and N₂ Lyman-Birge-Hopfield (LBH) band emissions that are used to determine thermospheric density profiles and state parameters related to thermospheric composition; specifically the thermospheric column O/N₂ ratio (symbolized as $\Sigma\text{O/N}_2$). This paper describes the algorithm concept that has been adapted and updated from one previously applied with success to limb data from the Global Ultraviolet Imager (GUVI) on the NASA Thermosphere Ionosphere Mesosphere Energetics and Dynamics (TIMED) mission. We also describe the requirements that are imposed on the ICON FUV to measure $\Sigma\text{O/N}_2$ over any 500-km sample in daytime with a precision of better than 8.7%. We present results from orbit-simulation testing that demonstrates that the ICON FUV and our thermospheric composition retrieval algorithm can meet these requirements and provide the measurements necessary to address ICON science objectives.

Keywords ICON Explorer mission · Thermosphere · Composition · Ultraviolet airglow

1 Introduction

The Ionospheric Connection Explorer (ICON) is a NASA mission that will answer long-standing questions about the source of equatorial ionospheric variability, the influence of

The Ionospheric Connection Explorer (ICON) mission
Edited by Doug Rowland and Thomas J. Immel

✉ A. W. Stephan
andrew.stephan@nrl.navy.mil

¹ U.S. Naval Research Laboratory, Washington, DC, USA

² George Mason University, Fairfax, VA, USA

³ U.S. Naval Research Laboratory (Voluntary Emeritus), Washington, DC, USA

⁴ Virginia Polytechnic and State University, Blacksburg, VA, USA

⁵ Space Sciences Laboratory, University of California-Berkeley, Berkeley, CA, USA

large-scale atmospheric waves, and the response of ion-neutral coupling to changes in solar and geomagnetic forcing. The emphasis on the intricate coupling not only across atmospheric boundaries but between ionized and neutral species within the ionosphere-thermosphere system itself dictates the importance of measuring the comprehensive state of both ionized and neutral constituents. To measure large-scale (greater than 1000 km) atmospheric waves and tides and their effects on the ionosphere, ICON mission goals specifically call out for the need to measure altitude profiles of O and N₂, and subsequently determine from them the ratio of column O to column N₂ (symbolized as $\Sigma\text{O}/\text{N}_2$) in the daytime thermosphere (Immel et al. 2018).

The ratio of the O column density to the N₂ column density, $\Sigma\text{O}/\text{N}_2$, is a geophysical parameter originally proposed by Strickland et al. (1995) for relating disk images of the O and N₂ FUV dayglow to thermospheric composition. (Disk observations imply that the entire emitting column is being viewed, as opposed to limb observations where the emission above some tangent altitude is measured.) They demonstrated that the vertical column density ratio, $\Sigma\text{O}/\text{N}_2$, is directly proportional to the intensity ratio of OI 135.6 nm to N₂ LBH viewed downward from satellite altitudes. Both emissions arise primarily from photoelectron impact, exciting atomic oxygen to the 2p⁴ ³P state and N₂ molecules to the a¹Π_g electronic level. There is additionally a contribution to O (2p⁴ ³P) excitation from radiative recombination of atomic oxygen ions in the ionosphere above about 300 km and a small contribution from dissociative excitation of O₂ at low altitudes. The Strickland et al. (1995) concept enabled for the first time a method for extracting quantitative information on the global variations of the thermospheric composition from Earth disk images. Disk images of the retrieved $\Sigma\text{O}/\text{N}_2$ can now easily be compared with any upper atmospheric model, whose number densities can be converted easily into the column density ratio defined by Strickland et al. (1995).

It is important to note that this geophysical parameter, developed as a means to relate disk images of FUV dayglow to a geophysical quantity for comparison to atmospheric model calculations, is more complex than quantities such as the number density ratio at a fixed altitude. Consequently, misunderstanding has arisen over its meaning—even among coauthors of the original concept paper (see Strickland et al. 2012 and Zhang and Paxton 2012). Our view of the physical reasoning behind the relationship between the disk-viewing 135.6/LBH emission ratio and $\Sigma\text{O}/\text{N}_2$ is that most of the solar EUV radiation that produces photoelectrons with sufficient energy to excite FUV radiation from O and N₂ is deposited where the (vertical) N₂ column density reaches 10¹⁷ cm⁻². Thus, the 135.6 and LBH column emissions originate mostly from the altitude region where the column densities are of this order and consequently provide a good measure of their ratios. Note that the O column density is also of this same order such that $\Sigma\text{O}/\text{N}_2$ is typically in the range of 0.3 to 1.5. The key point, and a source of the controversy, is that the interpretation and application of the relationship between emission ratio and column density ratio do not involve the altitude of the column base. Altitude only becomes a factor when introducing model atmospheres for comparison. While the reference altitude, typically 130–140 km, does change with exospheric temperature (e.g. Stephan et al. 2008), it is incorrect to attribute $\Sigma\text{O}/\text{N}_2$ variations directly to changes in the column base altitude—the variations are only due to the relative abundance of O relative to N₂ in the glowing column where the solar radiation is deposited.

Analysis of FUV data from the Global Ultraviolet Imager (GUVI) instrument on the NASA Thermosphere Ionosphere Mesosphere Energetics and Dynamics (TIMED) Explorer mission demonstrated sensitivity of $\Sigma\text{O}/\text{N}_2$ to dynamical processes in the thermosphere that can change the abundance of O relative to N₂ (e.g., Zhang et al. 2004; Meier et al. 2005; Crowley and Meier 2008; Meier et al. 2015). The inversion approaches used for retrievals of

$\Sigma\text{O}/\text{N}_2$ from GUVI data have also been applied to data from the Special Sensor Ultraviolet Limb Imager sensors on the DMSP F16-F19 satellite series (Dymond et al. 2017). Changes in $\Sigma\text{O}/\text{N}_2$ have also been linked to changes in F-region peak electron density (Strickland et al. 2001; Immel et al. 2001) and total electron content (Lean et al. 2011a), as would be expected from photochemical equilibrium.

The approach chosen by the ICON team to meet the requirement for high quality $\Sigma\text{O}/\text{N}_2$ (described in Immel et al. 2018) is to image the limb emissions of OI 135.6 nm within a 131–140 nm passband, and a segment of the molecular nitrogen Lyman-Birge-Hopfield band (N₂ LBH) from 152–162 nm. The resulting altitude profiles of the emission rates can be inverted to obtain the number density profiles of O and N₂ (Meier and Picone 1994). The column density ratio can then be found through vertical integration of the number densities and taking their ratio. Uncertainties in the radiance measurements can be mapped into the uncertainties in the data products following propagation of errors (Bevington and Robinson 1992).

The measurements will be made by the ICON Far-Ultraviolet spectrometer (ICON FUV) described in Mende et al. (2017). Briefly, the ICON FUV is a Czerny-Turner spectrographic imager that produces two-dimensional spectrally filtered images for each of the two passbands identified above, with a separate microchannel plate camera dedicated for each band. When operated on the daytime, the FUV instrument turret (used at night to align the field of view with the local magnetic field lines) is held fixed to align the imager to the port side of the ICON vehicle with the 24-degree vertical field of view aimed to cover 8 to 32 degrees below local horizontal. For the planned ICON orbit at 575 km, this alignment allows the imager to view tangent altitudes starting at 500 km and spanning down onto a region of the disk. The data are collected in 12-s exposures with pixels in the image offset in the horizontal direction and co-added onboard to compensate for motion of the spacecraft, resulting in six separate vertical (tangent altitude) stripes returned per daytime exposure, each corresponding to 3 degrees in horizontal extent (approximately 126 km at 140 km tangent altitude).

The present paper describes the algorithm that will be used to convert ICON FUV measurements into column O/N₂ data products. We demonstrate that the ICON FUV instrument, in conjunction with the algorithm described herein, will surpass the ICON mission requirement of 8.7% precision for the column O/N₂ density ratio with a 12-second duration exposure. This performance also is well within the horizontal range resolution of 500 km great circle that is traversed over the course of about a minute by the ICON FUV. Although our results show that co-adding successive exposures up to this horizontal range is not necessary to meet the 8.7% precision requirement, it does provide an additional margin to the performance results presented here.

2 Algorithm Concept

The ICON FUV inversion approach follows the GUVI limb imaging approach (Meier et al. 2015) by retrieving number (volume) densities, using the principles of Meier and Picone (1994). The GUVI algorithm included both the O and O₂ sources of 135.6 nm radiation, but did not account for radiative recombination of O⁺ + e radiative recombination. Consequently, inversions only used data from tangent altitudes up to about 300 km where the photoelectron impact source dominates. It is expected that ICON measurements taken from the lower latitudes may potentially include significant contributions from the ionospheric recombination source in the equatorial arcs. Thus, we have included radiative recombination

in the ICON algorithm for completeness, and to extend the range of usable data to higher tangent altitudes. Even though daytime ionospheric products will be retrieved, these are not a requirement for the ICON FUV. However, it will be possible to evaluate these products as context for the ICON EUV (Sirk et al. 2017) that does provide daytime ionospheric products (Stephan et al. 2017). It is also worth noting that the ICON orbit inclination of 27 degrees is sufficiently high that some observations will be outside the equatorial arc region and may not always contain a measurable ionospheric contribution. In the following, we first describe the neutral density inversion and then results from inclusion of the radiative recombination source.

Details of the methodology used to retrieve neutral densities from the GUVI data are given by Meier et al. (2015); consequently, only a brief summary of the inversion process will be provided here. From the altitude profiles of O and N₂ (along with O₂) returned by the inversion, the column ratios, $\Sigma\text{O}/\text{N}_2$, are obtained by first integrating the retrieved N₂ number density profile vertically downward to find the altitude at which the column density above equals 10^{17} cm^{-2} . The O column density above this N₂ level is then computed and the ratio taken. Thus, although $\Sigma\text{O}/\text{N}_2$ was originally conceived as an observational quantity to be retrieved from disk images, it can be obtained equally well from limb observations (and models).

The ICON limb neutral density retrieval algorithm begins with a parameterized forward model that predicts the expected emission rates as a function of look angle for direct comparison to the FUV measurements. The model incorporates a first principles representation of the photoelectron excitation rates and radiative transfer of photons based on a parameterization of the thermospheric densities obtained using the NRLMSISE00 model (Picone et al. 2002). Following Meier and Picone (1994) and Meier et al. (2015), the parameters used in our algorithm are a scalar applied to the $F_{10.7}$ solar radio flux input to NRLMSISE00 that effectively adjusts the altitude profiles of the species, and three altitude-independent scalars of the resulting N₂, O₂ and O density profiles to establish the magnitudes. There are two additional magnitude scalars applied to the computed 135.6 and LBH emission rates to account for any systematic uncertainties in the instrument calibration or magnitude of the photoelectron impact excitation cross section. These six parameters of the forward model are then iteratively adjusted using the Levenberg-Marquardt method of nonlinear least squares fitting (Marquardt 1963) until the output produces the optimal match to the ICON FUV measurements. This method of using a weighted non-linear least squares fit of a model to data is called Discrete Inverse Theory (Menke 1989), or Optimal Estimation.

As described in Meier et al. (2015), the initial excitation rate, j_O , is given by the product of the g -factor of the photoelectron-excited emission and the species number density (N_O or N_{N_2}). The g -factor, $g(\mathbf{r})$, at location \mathbf{r} along the line of sight through the atmosphere defines the number of excitations per second per atom and is determined from the integral over energy of the product of the photoelectron impact excitation cross section, σ , and the photoelectron flux (electron $\text{cm}^{-2} \text{ s}^{-1} \text{ eV}^{-1}$), Φ :

$$g(\mathbf{r}) = \int \sigma(E)\Phi(E, \mathbf{r})dE. \quad (1)$$

The column emission rates observed by the ICON FUV OI 135.6 nm (short wavelength, SW) and N₂ LBH (long wavelength, LW) channels are then described by the following

integrals along the line of sight path segment ds :

$$4\pi I_{SW} = \int (j_O + j_{ms}) \sum_{i=135.6}^{135.8} B_i [e^{-\tau_{O_2}^i} T(\tau_O^i)] ds + \int j_{N_2} \int B_{SW}(\lambda) e^{-\tau_{O_2}(\lambda)} d\lambda ds \quad (2)$$

$$4\pi I_{LW} = \int j_{N_2} \int B_{LW}(\lambda) e^{-\tau_{O_2}(\lambda)} d\lambda ds,$$

where j_O and j_{N_2} are the initial volume emission rates for OI 135.6 nm and j_{ms} is the additional contribution to the 135.6 nm emission from multiple scattering. Extinction along the path from the emitting region to ICON by molecular oxygen is accommodated by $e^{-\tau_{O_2}}$, and self-absorption (resonant scattering out of the emission path by O) represented by the Holstein transmission function, $T(\tau_O)$ (see Meier 1991), which explicitly includes the wavelength dependence of the resonant scattering cross section and the volume emission rate. The sum over wavelength index, i , accounts for the doublet nature of the O ($^5S_2 \rightarrow ^3P_{1,2}$) transition at their respective wavelengths, 135.85123 and 135.5977 nm. B_i is the fraction of the emissions emitted in each line of the doublet. The second (double) integral in the SW band takes into account the underlying emission from the N₂ LBH bands that falls within the passband. In this expression, B_{SW} represents the wavelength (λ) dependent branching ratio of the total N₂ LBH excitation that falls within the SW passband, calculated as the product of 0.8871 that corresponds to the fraction of excitations of the N₂ ($a^1\Pi_g$) state that result in LBH emissions (i.e., that do not predissociate) (Ajello and Shemansky 1985), and the fraction of the LBH vibrational transition bands that falls within the SW channel. The extinction factor for each emission by O₂, $e^{-\tau_{O_2}}$, includes a detailed representation of the O₂ absorption cross section as a function of wavelength and temperature (Gibson et al. 1983; Gibson and Lewis 1996; private communication between R.R. Meier and S.T. Gibson, 2005). The full calculation for ICON includes the rather small contribution from photoelectron impact dissociative excitation of O₂ (see Sect. 4). Because the excited O atoms from this process are kinetically hot, most of the emission resides outside the Doppler core of the thermal line profile and extinction by self-absorption is negligible.

The lower integral in (2) is the LBH band emission within the long wavelength channel, LW. Definitions of the various factors in the LW equation are analogous to those for the SW case. Note that the molecular oxygen number density can also be retrieved from the limb measurements over a limited altitude range because the O₂ optical depth is the product of the absorption cross section and the O₂ column density between ICON and the emitting volume element along the path, s .

To correctly simulate the emission rate observed by the FUV instrument Eq. 2 must include the specifics of the FUV instrument responsivity across each passband. Thus, the simulated column emission rates must include $R(\lambda)$, the instrument responsivity in the SW and LW channels normalized so that the peak responsivity is unity. Equation (2) thus becomes:

$$4\pi I_{SW} = \int (j_O + j_{ms}) \sum_{i=135.6}^{135.8} R_{SW}(\lambda_i) B_i [e^{-\tau_{O_2}^i} T(\tau_O^i)] ds$$

$$+ \int j_{N_2} \int R_{SW}(\lambda) B_{SW}(\lambda) e^{-\tau_{O_2}(\lambda)} d\lambda ds \quad (3)$$

$$4\pi I_{LW} = \int j_{N_2} \int R_{LW}(\lambda) B_{LW}(\lambda) e^{-\tau_{O_2}(\lambda)} d\lambda ds.$$

The wavelength-integrated fractions of the total LBH emission that fall within the SW and LW channels, $\int R_{SW,LW}(\lambda) B_{SW,LW}(\lambda) d\lambda$, are 0.122 and 0.0681, respectively.

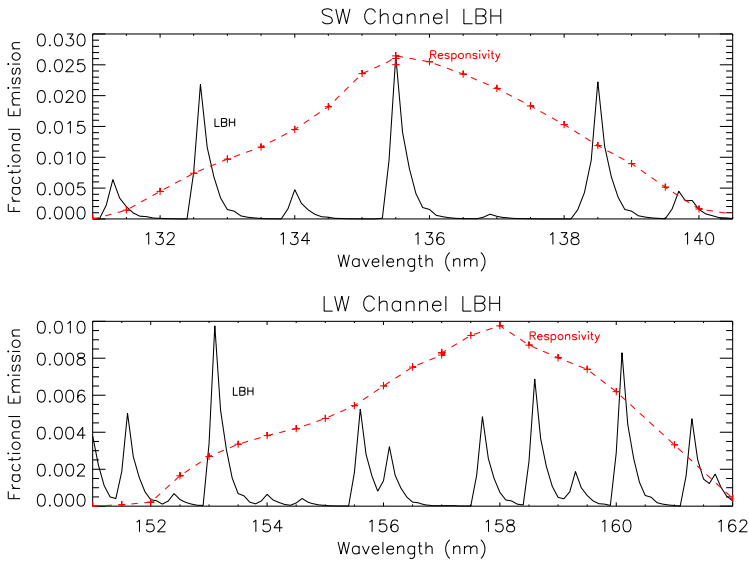


Fig. 1 Fraction of LBH in SW and LW FUV channels. *Black* is the spectral distribution of the fractional emission and *red* is the FUV instrument channel responsivities, normalized to the peak emission within each channel. The wavelength resolution is 0.1 nm and the temperature is 500K. There is no O_2 extinction for this example. The absolute responsivity is 39.7 and 14.1 counts/science pixel/s/kR for the SW and LW channels, respectively, for each of the 6 vertical profiles collected simultaneously for each channel. A “science pixel” is defined as 1 binned vertical resolution element (equal to 4 pixels on the CCD), corresponding to a segment of the field of view 0.093 deg (*vertical*) by 3.0 deg (*horizontal*) (see also Table 8 in Mende et al. 2017)

The fractional emission rates without O_2 extinction are shown in Fig. 1 for the SW channel (upper) and LW channel (lower) panels. The black spectra are the fractional LBH emission before multiplication by B . The red dashed curves are the normalized instrument responsivity (Mende et al. 2017).

3 Algorithm Requirements

In order to meet the ICON science objectives, the algorithm must be able to invert the ICON FUV daytime measurements to obtain the number density profiles of O and N_2 . The measurement concept requires sunlit conditions, and the algorithm forward model specifically requires that all parts of each line of sight in the altitude profile for which emission contributions will be determined are located at positions with solar zenith angles less than 90 degrees. While products will be generated for all such daytime measurements, in practice the accuracy of the algorithm has been found to deteriorate once the solar zenith angle at the tangent point becomes larger than about 70 degrees (Meier et al. 2015). This is a consequence of the migration of the emission layer to higher altitudes with increasing solar zenith angle, thereby reducing the sensitivity of the analysis to the molecular species.

While the ICON science objectives require a minimum temporal resolution of one minute, equivalent to 500 km horizontal sampling, in practice the sampling cadence (for a single image containing six altitude profiles or stripes) will be every 12 seconds, meaning that spectra could be co-added to improve the signal-to-noise of each profile, or a set of profiles can be merged after processing to the Level 2 stage by this algorithm. Co-adding

data would involve altitude correction between stripes because a given pixel number within a stripe has a slightly different altitude than the same pixel number in the other stripes. However, as we show later, the science requirements will be met through inversion of a single image stripe, so combining data between stripes will not be necessary. The algorithm will be able to determine the vertical profile between 100 km and up to 500 km. The needs of the algorithm to meet this measurement objective drive, in part, the instrument requirements described by Mende et al. (2017).

Previous and current tests have all confirmed that the retrieved altitude profiles, and consequently the $\Sigma\text{O}/\text{N}_2$ products, are essentially independent of the solar flux (e.g. Meier and Picone 1994) and will only be systematically offset from the “truth” if they are (1) retrieved using physically unrealistic solar fluxes, or (2) if there are serious systematic differences in the photoionization cross-sections used to generate the airglow profiles. For ICON, we have used the state-of-the-art NRLSSI-EUV empirical solar model (Lean et al. 2011b; private communication between R.R. Meier and J.L. Lean, 2017) to provide a physically realistic sun to minimize the former concern.

4 Algorithm Verification

A wide variety of tests were performed to ensure that the ICON FUV daytime $\Sigma\text{O}/\text{N}_2$ algorithm is operating properly. Additional verification of the algorithm was completed through a flight-like test using a series of end-to-end simulations conducted by the ICON team. The combination of these quantitative tests, coupled with the extensive heritage of the core algorithm used for successfully inverting data from TIMED/GUVI, as well as (SSULI) (Dymond et al. 2017) and SSUSI (Paxton et al. 1992), including regions of depleted $\Sigma\text{O}/\text{N}_2$ during large geomagnetic storms (Meier et al. 2005; Crowley and Meier 2008), gives us confidence that the algorithm is appropriate for analyzing a wide range of atmospheric conditions that will be encountered by ICON.

First, the ICON team generated a representative set of ICON positions and FUV viewing conditions for a single orbit that included 194 FUV limb images during the daytime (solar zenith angle less than 80 degrees). These were then ingested by the first principles forward model to produce noise-free OI 135.6 nm and N₂ LBH band limb emission rates (the “true” radiances). The forward model uses the SEE-based (Solar EUV Experiment; Woods et al. 2008) NRLSSI-EUV solar model, the parameterized NRLMSISE00 neutral density model, and the Atmospheric Ultraviolet Radiance Integrated Code (AURIC) photon and photoelectron excitation model (Strickland et al. 1999). An example of a limb scan predicted by the forward model with the ICON FUV viewing conditions is shown in Fig. 2. For this illustration, the solar 10.7 cm flux was set to 100 SFU (1 SFU = 10^4 Jansky = 10^{-22} Wm⁻² Hz⁻¹). We have also carried out simulations for a solar 10.7 cm flux of $F_{10.7} = 76$, to test the algorithm robustness at solar minimum, corresponding to the range of conditions that ICON is likely to experience. Geomagnetic activity was low. The upper panels display the “noiseless” column emission rates for the SW (left) and LW (right) channels. Individual contributions to the total signal from electron impact photoelectron impact excitation of O, dissociative excitation of O₂ and LBH bands present within the passband are individually plotted as well as their total. LBH emission is the only contributor to the LW channel.

Next the noiseless synthetic data for all limb scans in the test orbit were passed through an instrument simulator (model) that generated a full set (194 exposures during the daytime portion of the orbit) of FUV images at 12-s cadence, each containing six stripes (six 256-pixel limb altitude profiles). Each of the 194×6 limb profiles for each channel therefore

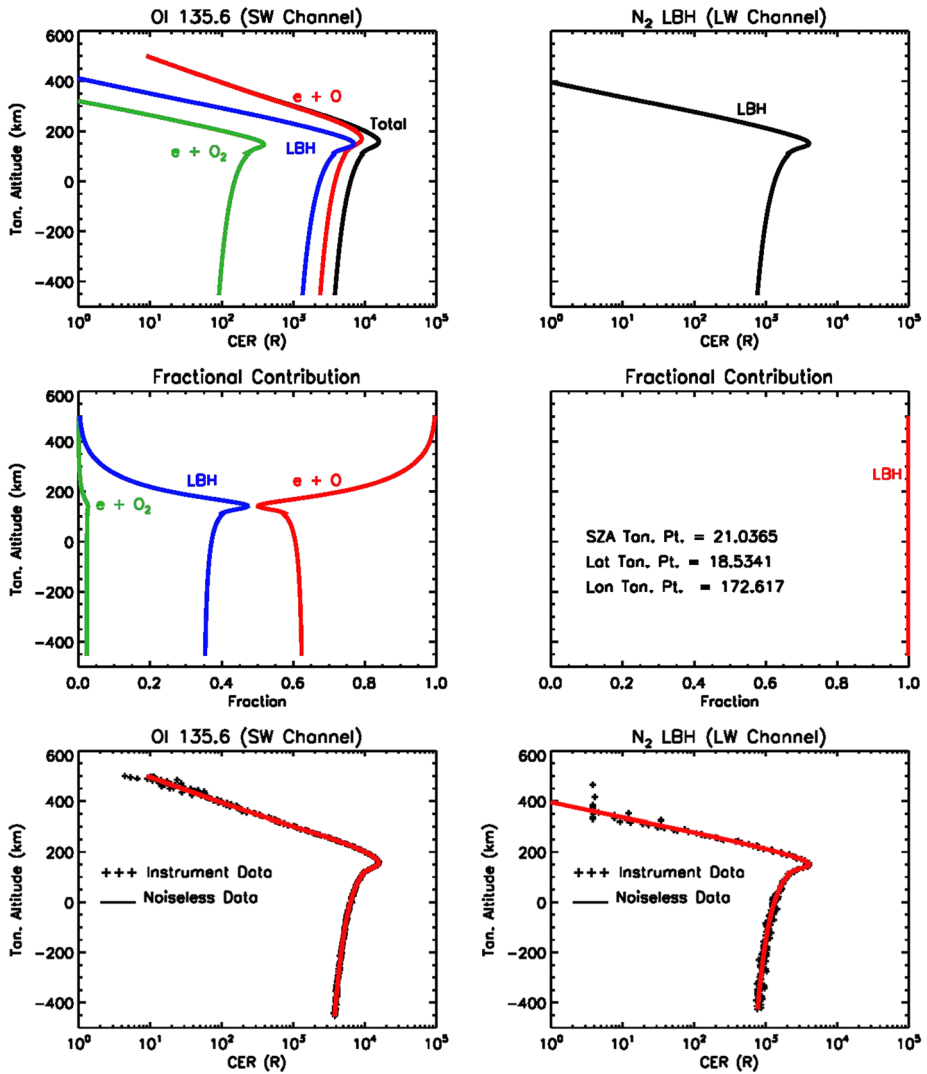


Fig. 2 The *upper panels* show an example of the forward-modeled radiances for the ICON FUV short wavelength (SW) 135.6 nm channel (*left*) and the long wavelength (LW) N₂ LBH 157 nm channel (*right*). The *middle panels* show the fractional contribution from each emission source. The *lower panels* show the radiances after passing the results from the *upper panels* through the ICON FUV instrument model (see Mende et al. (2017) for instrument details)

consist of flight-like representations of the Level 1 data products with their concomitant counting statistics and signal digitization. The bottom panels of Fig. 2 show plots of the radiances before and after passing through the instrument model. (See Mende et al. (2017) for a more detailed explanation of the mapping from dayglow scene through the optics to the CCD and the 6 stripes.) Except at the highest altitudes, where the airglow brightness is very low, the instrument responsivity produces high fidelity simulated data. In general, the number of CCD pixels within each altitude sample varies, but the mean value for the 135.6 nm

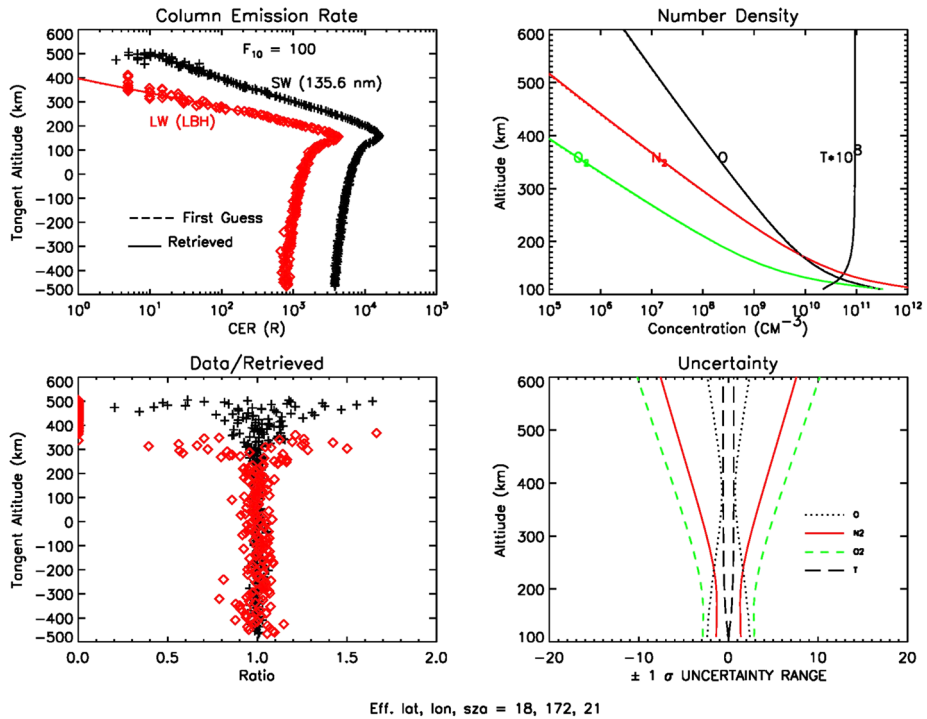


Fig. 3 This figure shows results from the inversion of the radiance profiles shown in Fig. 2. The synthetic data in the *upper left panel* are given by the labeled symbols for SW and LW channels. The *upper right panel* shows the initial guess and retrieved number densities and temperature (K). The initial guesses given by the *dashed lines* are difficult to see because they are very close to the final retrievals (*solid lines*). The *lower left panel* shows the ratio of the data to the retrieved radiances. The *lower right* shows the uncertainties in each of the retrieved quantities after propagating the measurement uncertainties through the algorithm

channel is about 11 CCD pixels and 14 for the LBH channel. The number of altitude samples within each image stripe also varies, and can be different for the two channels because not all of the CCD is illuminated by the optics. The number of altitude samples across the 6 stripes ranges from 226 to 251 out of a possible 256. For example, two of the lowest and three of the highest pixels (i.e., tangent altitudes) from Stripe 3 are regions where the curved grating edges result in no source pixels in the square output detector image—these are marked as Not-a-Number (NaN) in the Level 1 data to distinguish them from pixels with real values of zero counts, and are removed prior to inversion. The exposure time for each 6-stripe image is 12 s.

The inversion algorithm was then used to process these data in a flight-like test. The first guess radiances corresponding to the geophysical conditions and location before (i.e., the noiseless data or “truth” given by dashed lines) and after processing through the ICON FUV instrument model (discrete symbols) are plotted in the upper left panel of Fig. 3. In this simulation, the initial guess is the same as the noise-free radiances generated in the first step, while operationally this is determined by inputs for solar and geophysical conditions at the time of the measurement. Our extensive testing of the algorithm over the past decade, including for ICON, has found that convergence to a solution is robust with any geophysically-reasonable starting point. The solid lines represent the CERs retrieved by the algorithm. They are very close to the noiseless (first guess) values, rendering the latter dif-

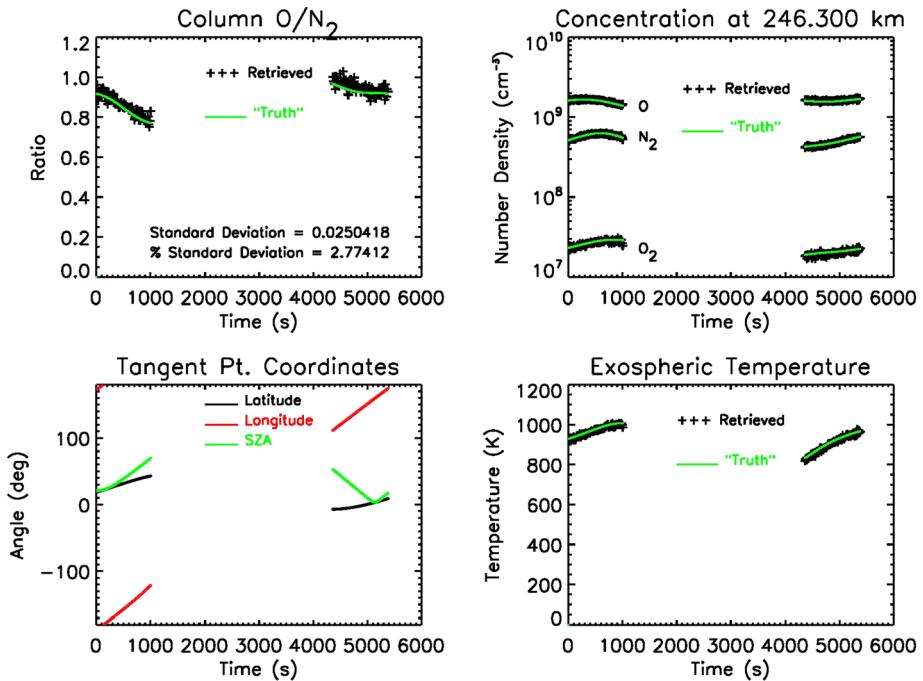


Fig. 4 Plot of the full orbit of retrieved $\Sigma O/N_2^2$ (black) vs. truth (green) from simulated ICON FUV instrument data (upper left) at the location shown (lower left). Retrieved composition at 246 km (upper right) and exospheric temperature (lower right) in comparison to the “truth” input values are shown

difficult to see on the condensed log-plot. The lower left panel is the ratio of the simulated instrument data divided by the retrieved emission rates, providing a visual measure of the goodness of fit. The upper right panel shows the first guess model atmosphere (dashed) and the retrieved concentrations. Again, they are very close. Their uncertainties based on propagation of the random uncertainties in the data are displayed in the lower right panel. The column O/N_2 ($\Sigma O/N_2$) for this limb scan is 0.94 with an uncertainty of about 2%. This is an excellent result, given the measurement requirement of 8.7%.

Retrievals of $\Sigma O/N_2$ from the entire orbit are summarized in the upper left panel of Fig. 4. The retrieved values given by the symbols are close to the “truth”, (noiseless column emission rates). The standard deviation of the retrieved values from the “truth” gives an estimate of the orbital average random uncertainty, about 2.8%. For illustration, the retrieved concentration at 246 km and the corresponding exospheric temperature are compared with the “truth” in the right panels. Repeating this simulation for $F_{10.7} = 76$ increases the orbital average a modest amount, to 3.2% but still well within the ICON requirement. Experience with GUVI has shown that the uncertainty increases with solar zenith angle, especially at values greater than about 65 deg. This test with the ICON algorithm has no limb scan with $\Sigma O/N_2$ uncertainties greater than 2σ and there are only two limb scans collected at solar zenith angles between 65 and 70 degrees with 5–6% uncertainty. These examples demonstrate that even the inversion of a single stripe limb image will meet the science requirements even during times near minimum solar activity and that the ICON FUV will be able to easily achieve its goal for measuring $\Sigma O/N_2$ to 8.7% precision over 500 km.

While the ICON science objectives do not require FUV disk measurements, there are actually some 100 pixels in the strip images that view the full radiating column below the horizon. These observations could easily be converted into the traditional heritage (e.g., GUVI) disk $\Sigma O/N_2$ products using the Strickland et al. (1995) approach. Such an analysis could be valuable as a validation tool for the limb measurements (e.g. Stephan et al. 2008). Additional independent validation will be performed on-orbit using the approach employed with GUVI, specifically comparing ICON observations with other simultaneous ground and space-based measurements, including GUVI and SSULI. Comparisons can also be made with satellite drag and accelerometer total density measurements, ionospheric inferences using the Richards method of inferring neutral composition required to explain ionosonde and radar observations of the electron density (Richards et al. 2010), and any other data available.

5 Radiative Recombination

Because the ICON satellite will be in a relatively low inclination orbit of about 27 degrees, the FUV instrument will spend a significant part of the orbit viewing the equatorial ionosphere and the tropical arcs. These large increases in oxygen ion and electron densities on either side of the geomagnetic dip equator lead to radiative recombination that produces correspondingly bright FUV emissions, including the OI 135.6 nm emission. At night, this ionospheric source is the primary contributor to the emission (aside from a small secondary source due to mutual neutralization, $O^+ + O^-$, which we can ignore on the daytime because it occurs at lower altitudes where photoelectron impact excitation is far brighter) and is used to infer the state of the nighttime ionosphere (Kamalabadi et al. 2018).

The rate of O (5S) excitation from radiative recombination as a function of altitude, z , is given by:

$$j_{RR}(z) = \alpha_{135.6} N_{O^+}(z) N_e(z) \quad (4)$$

where $\alpha_{135.6}$ is the partial recombination rate coefficient into the 5S state, and the N represents the number densities of each indicated species. We use the rate coefficient recommended by Melendez-Alvira et al. (1999). In the F-region, the electron density is closely approximated by the O^+ density, so j_{RR} becomes proportional to the square of the electron density. The RR source term, Eq. (4), is simply included in the j_o term in Eqs. (2) and (3).

We have parameterized the electron density by a Chapman function,

$$N_e(z) = N_e(z_0) \exp \left[\frac{1}{2} \left(1 - \frac{(z - z_0)}{H} - e^{-\frac{(z - z_0)}{H}} \right) \right] \quad (5)$$

The three parameters of the Chapman function are the maximum electron density, $N_e(z_0)$, the peak altitude, z_0 , and the scale height, H . In the ionospheric vernacular, $N_e(z_0)$ is NmF₂, z_0 is hmF₂. Following the neutral density approach, the inversion algorithm uses scalars for each of these three parameters. Uncertainties in the electron density are obtained by propagating the retrieved uncertainties of three parameters. Thus, the inversion from each limb scan returns a total of nine parameters: four for the neutral densities, two for the instrument channel magnitudes and three for the ionosphere. Because the number of measurement samples in each limb profile is of the order 256, the inversion problem is still well-overdetermined.

We repeated the previous test of the neutral density retrievals, but with the ionospheric source included. The noiseless radiances were created using estimates of the unscaled three

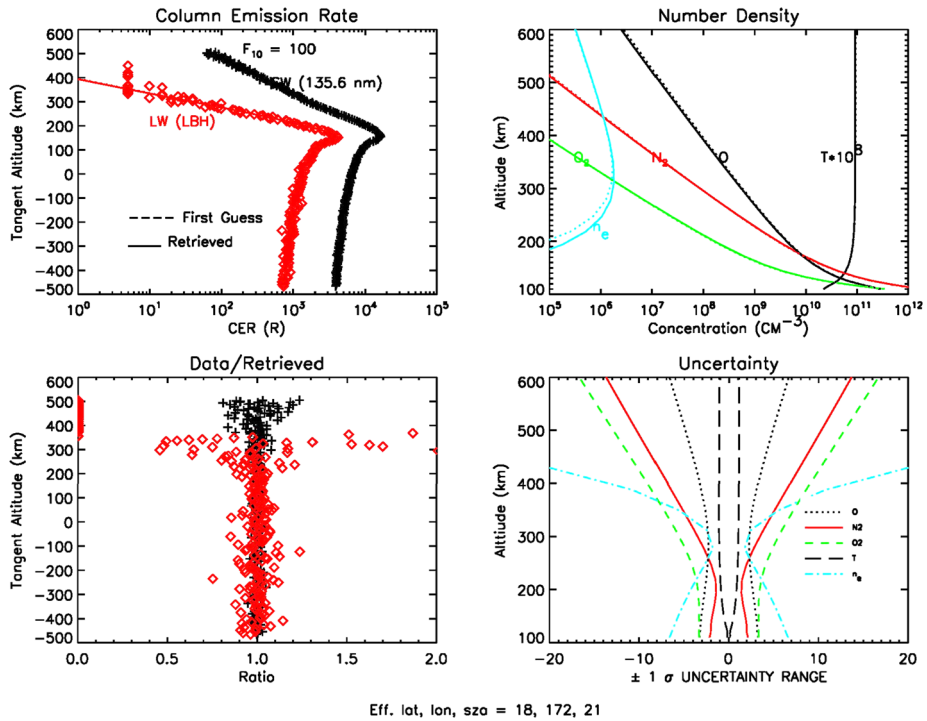


Fig. 5 Same as Fig. 3, with the inclusion of the ionospheric radiative recombination term in the forward model and ionospheric parameters in the retrieval. The electron density profile is included (*aqua colored line*) in the *upper right panel*, and its uncertainty included in the *lower right panel*

Chapman parameters from the IRI values appropriate to the limb scan conditions. As before, instrument effects are applied to the noiseless radiances to simulate “true” measurements that we process to retrieve the optimal parameters. Figure 5 shows a repeat of Fig. 3 but with the radiative recombination source included in the 135.6 channel radiance (upper left panel), as well as the electron density profile (upper right) and its uncertainty (lower right). The ionospheric source causes a noticeable increase in slope of the OI 135.6 nm emission around 300 km, compared with that of Fig. 3, confirming the restrictions implemented for the GUVI algorithm. As a result, the uncertainties of the neutral density profiles and temperature increase, especially at higher altitudes. Nonetheless, $\Sigma O/N_2$ changes by less than 2% from that of Fig. 3, which is within its retrieval uncertainty for this limb scan example.

The full orbital perspective is shown in Fig. 6, which is analogous to Fig. 4 but this time including the radiative recombination source. The orbital average uncertainty of $\Sigma O/N_2$ increases from about 2.8% to 3.1%, still well within the prescribed ICON requirement.

A similar plot for the retrieved Chapman parameters in Fig. 7 demonstrates that during parts of the orbit, the electron density retrieval is remarkably good. Its uncertainties, shown in red, only become large when NmF2 drops below 10^5 cm^{-3} . HmF2 is more difficult to retrieve, but the precision of the retrieval is again very good for the part of the orbit where NmF2 and HmF2 are larger. The scale height retrieval in the lower right panel is also reasonably good, although the propagated uncertainty into electron density shows increases away from the HmF2 altitude.

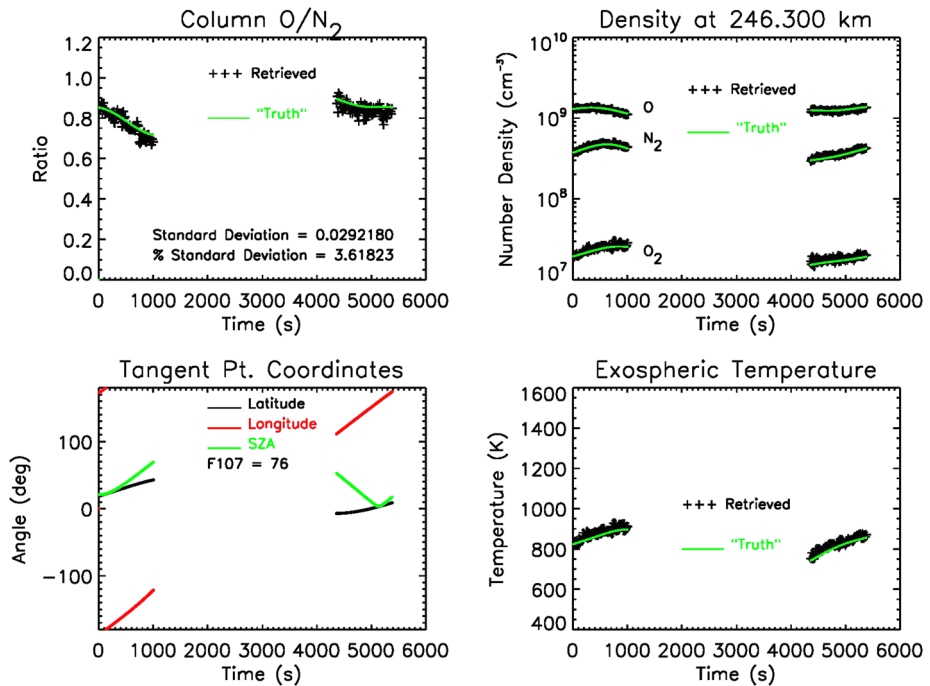


Fig. 6 Same as Fig. 4, retrieved with the inclusion of the ionospheric radiative recombination term and ionospheric scaling parameters included in the forward model

The reason for the relatively high quality of the electron density retrieval in the presence of the stronger dayglow signal on the bottom side is that IRI predicts NmF2 greater than 10^6 cm^{-3} for much of the orbit, even for the relatively low level of solar activity. Since the radiative recombination source is proportional to the square of the electron density, higher NmF2 rapidly increases the ionospheric emission rate. As before, we also repeated this exercise for very low solar activity ($F_{10.7} = 76$). Although the $\Sigma\text{O}/\text{N}_2$ uncertainty only increased from 3.1% to 3.6%, the Chapman parameters uncertainties increased somewhat more.

We conclude that the presence of emission from $\text{O}^+ + e$ radiation on the topside of the electron-impact emission profile does not significantly worsen the uncertainty in retrievals of the neutral density profiles and the required operational parameter, $\Sigma\text{O}/\text{N}_2$. As long as the electron density peak value is above about 10^6 cm^{-3} , good quality retrievals of its parameters are possible, although it seems likely that this conclusion will also be dependent on the F-region height—if the height is too low, the emission will be overwhelmed by the thermospheric emission and the uncertainty in the electron densities will become large.

6 ICON FUV Level 2 Data Products

The ICON Level 2 (L2) data products produced by this algorithm for the FUV measurement will include the key ancillary information from the Level 1 (L1) data files, the retrieved O, N₂, and O₂ densities and temperature profiles and the corresponding $\Sigma\text{O}/\text{N}_2$ values along with uncertainties in each. Additional quality flags will be included, along with flags passed through from the L1 data that are relevant to these L2 products, that will identify departures

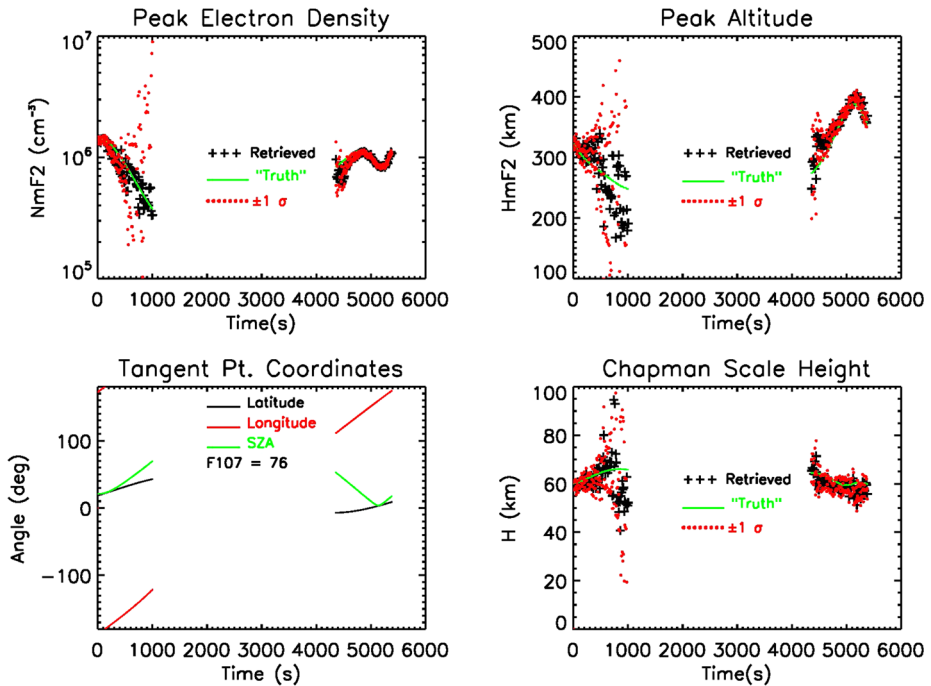


Fig. 7 Retrieved Chapman parameters. *Upper left* shows the retrieved NmF2 (+) and its uncertainty (*red dots*). The initial guess from IRI is shown as the “truth” in *green*. *Upper right*: same legend but for HmF2. *Lower left* are the orbital values. *Lower right* is the scale height, again with the same legend

from the expected high quality of the retrievals, along with other data quality metrics (e.g. convergence issues, model parameters driven to imposed limits that are presumably unphysical, and high χ^2 values from the fit) that users should consider when conducting an analysis with the L2 products.

Although not a requirement for the ICON FUV, we also plan to evaluate the retrieved electron density information and include this in the L2 products if it is determined to be of reasonable scientific quality and value. Additionally, we will provide an estimate of the solar EUV energy flux required to produce the airglow value by using the absolute magnitude of either of the column emission rates. Strickland et al. (1995) defined this quantity, Q_{EUV} , as the integral over wavelength of the solar spectral irradiance from 1 to 45 nm, in units of (W m^{-2}). See Meier et al. (2015) for more details on this data product. Again, this is not a required data product for the ICON mission, but will be included as it is inherently available as part of the inversion process.

7 Considerations for Algorithm Enhancement

There are a number of areas where the algorithm may be able to benefit by upgrades that could provide scientific information beyond the ICON science goals. The ICON team will continue to evaluate these options. Several options are already under consideration.

One obvious and high-priority target is the incorporation of a separate algorithm to analyze the disk observations because it provides both a separate check on the limb results

(e.g. Stephan et al. 2008), and a more direct comparison to the data that will be available from NASA's Global-scale Observations of the Limb and Disk Mission (GOLD) (Eastes et al. 2017). Disk observations view a column of glowing atmosphere with no altitude information. Consequently, a disk algorithm (Strickland et al. 1995) follows an approach much different from the limb algorithm, using a simple relationship between the ratio of the measured O and N₂ emission rates and $\Sigma\text{O}/\text{N}_2$. A similar relationship can be derived for ICON viewing conditions using this same prescription.

Ultimately, an algorithm containing both FUV and EUV instrument observations would be highly beneficial. A four or five color algorithm that merges the current algorithm with the daytime ionosphere algorithm (Stephan et al. 2017) could, in principle, lead to self-consistent retrievals of both the neutral atmospheric and the F-region electron densities. Such an approach would be a direct and natural follow-on from the evaluation of the daytime ionospheric products returned by this FUV algorithm and those returned from the independent analysis of the EUV data.

8 Summary

The NASA Ionospheric Connection Explorer (ICON) mission will use an updated version of the GUVI limb algorithm to obtain the daytime thermospheric composition as a function of altitude and subsequently the required $\Sigma\text{O}/\text{N}_2$. The principal changes from the GUVI algorithm (Meier et al. 2015) are customization for the ICON orbit and viewing conditions, inclusion of the radiative recombination 135.6 nm emission from the daytime ionosphere, and implementation of the FUV instrument characteristics. Composition and column densities will be retrieved from OI 135.6 and N₂ LBH emissions measured on the limb by the Far Ultraviolet (FUV) spectrograph. Pre-flight simulations of ICON FUV measurements over a representative orbit have been conducted that show the algorithm is able to reproduce $\Sigma\text{O}/\text{N}_2$ to far better than 8.7% precision, over a 60-second integration corresponding to a 500 km arc. The estimated average uncertainty in the column density ratio is of order 3–4% from random counting statistics within a 12-second integration using a single stripe (out of 6 in each limb image). Thus, the design and verification testing of simulated ICON FUV flight data demonstrate that the algorithm successfully reproduces the “true” atmospheric composition, and by inference that the ICON FUV is able to measure the dayglow with fidelity sufficient to easily meet the performance requirements of the NASA ICON mission.

Acknowledgements ICON is supported by NASA's Explorers Program through contracts NNG12FA45C and NNG12FA42I. We acknowledge the input and feedback from the many scientists who have contributed to the evolution of this work, with specific acknowledgement to the support provided by Douglas P. Drob and J. Michael Picone. RRM thanks the Civil Service Retirement System for partial support.

References

- J.M. Ajello, D.E. Shemansky, A reexamination of important N₂ cross sections by electron impact with application to the dayglow: the Lyman–Birge–Hopfield band system and NI (119.99 nm). *J. Geophys. Res.* **90**(A10), 9845–9861 (1985). <https://doi.org/10.1029/JA090iA10p09845>
- P.R. Bevington, D.K. Robinson, *Data Reduction and Error Analysis for the Physical Sciences*, 2nd edn. (McGraw-Hill, New York, 1992)
- G. Crowley, R.R. Meier, Disturbed O/N₂ ratios and their transport to middle and low latitudes, in *Midlatitude Ionospheric Dynamics and Disturbances*, ed. by P.M. Kintner et al. (Am. Geophys Union, Washington, 2008). <https://doi.org/10.1029/181GM20>

- K.F. Dymond, A.C. Nicholas, S.A. Budzien, C. Coker, A.W. Stephan, D.H. Chua, The Special Sensor Ultraviolet Limb Imager instruments. *J. Geophys. Res. Space Phys.* **122**, 2674–2685 (2017). <https://doi.org/10.1002/2016JA022763>
- R.W. Eastes, W.E. McClintock, A.G. Burns et al., The Global-scale Observations of the Limb and Disk (GOLD) mission. *Space Sci. Rev.* (2017). <https://doi.org/10.1007/s11214-017-0392-2>
- S.T. Gibson, B.R. Lewis, Understanding diatomic photodissociation with a coupled-channel Schrodinger equation model. *J. Electron Spectrosc. Relat. Phenom.* **80**, 9–12 (1996). [https://doi.org/10.1016/0368-2048\(96\)02910-6](https://doi.org/10.1016/0368-2048(96)02910-6)
- S.T. Gibson, H.P.F. Gies, A.J. Blake, D.G. McCoy, P.J. Rogers, Temperature dependence in the Schumann-Runge photoabsorption continuum of oxygen. *J. Quant. Spectrosc. Radiat. Transf.* **30**, 385–393 (1983). [https://doi.org/10.1016/0022-4073\(83\)90101-2](https://doi.org/10.1016/0022-4073(83)90101-2)
- T.J. Immel, S.L. England, S.B. Mende, R.A. Heelis, C.R. Englert, J. Edelstein, H.U. Frey, E.J. Korpela, E.R. Taylor, W.W. Craig, S.E. Harris, M. Bester, G.S. Bust, G. Crowley, J.M. Forbes, J.-C. Gérard, H.M. Harlander, J.D. Huba, B. Hubert, F. Kamalabadi, J.J. Makela, A.I. Maute, R.R. Meier, C. Raftery, P. Rochus, O.H.W. Siegmund, A.W. Stephan, G.R. Swenson, S. Frey, D.L. Hysell, A. Saito, K.A. Rider, M.M. Sirk, The ionospheric connection explorer mission: mission goals and design. *Space Sci. Rev.* **214**, 13 (2018). <https://doi.org/10.1007/s11214-017-0449-2>
- T.J. Immel, G. Crowley, J.D. Craven, R.G. Roble, Dayside enhancements of thermospheric O/N₂ following magnetic storm onset. *J. Geophys. Res.* **106**(A8), 15471–15488 (2001). <https://doi.org/10.1029/2000JA000096>
- F. Kamalabadi, J. Qin, B. Harding, D. Iliou, J. Makela, R.R. Meier, S.L. England, H.U. Frey, S.B. Mende, T.J. Immel, Inferring nighttime ionospheric parameters with the Far Ultraviolet Imager onboard the Ionospheric Connection Explorer. *Space Sci. Rev.* (2018)
- J.L. Lean, R.R. Meier, J.M. Picone, J.T. Emmert, Ionospheric total electron content: global and hemispheric climatology. *J. Geophys. Res.* **116**, A10318 (2011a). <https://doi.org/10.1029/2011JA016567>
- J.L. Lean, T.N. Woods, F.G. Eparvier, R.R. Meier, D.J. Strickland, J.T. Correira, J.S. Evans, Solar extreme ultraviolet irradiance: present, past, and future. *J. Geophys. Res.* **116**, A01102 (2011b). <https://doi.org/10.1029/2010JA015901>
- D.W. Marquardt, An algorithm for least-squares estimation of nonlinear parameters. *J. Soc. Ind. Appl. Math.* **II**(2), 431–441 (1963). <https://doi.org/10.1137/0111030>
- R.R. Meier, Ultraviolet spectroscopy and remote sensing of the upper atmosphere. *Space Sci. Rev.* **58**, 1–186 (1991). <https://doi.org/10.1007/BF01206000>
- R.R. Meier, J.M. Picone, Retrieval of absolute thermospheric concentrations from the far UV dayglow: an application of discrete inverse theory. *J. Geophys. Res.* **99**(A4), 6307–6320 (1994). <https://doi.org/10.1029/93JA02775>
- R. Meier, G. Crowley, D.J. Strickland, A.B. Christensen, L.J. Paxton, D. Morrison, C.L. Hackert, First look at the 20 November 2003 superstorm with TIMED/GUVI: comparisons with a thermospheric global circulation model. *J. Geophys. Res.* **110**, A09S41 (2005). <https://doi.org/10.1029/2004JA010990>
- R.R. Meier et al., Remote sensing of Earth's limb by TIMED/GUVI: retrieval of thermospheric composition and temperature. *Earth Space Sci.* **2**, 1–37 (2015). <https://doi.org/10.1002/2014EA000035>
- D.J. Melendez-Alvira, R.R. Meier, J.M. Picone, P.D. Feldman, B.M. McLaughlin, Analysis of the oxygen nightglow measured by the Hopkins Ultraviolet Telescope: implications for ionospheric partial radiative recombination rate coefficients. *J. Geophys. Res.* **14**, 901 (1999). <https://doi.org/10.1029/1999JA900136>
- S.B. Mende, H.U. Frey, K. Rider, C. Chou, S.E. Harris, O.H.W. Siegmund, S.L. England, C.W. Wilkins, W.W. Craig, P. Turin, N. Darling, T.J. Immel, J. Loicq, P. Blain, E. Syrstadt, B. Thompson, R. Burt, J. Champagne, P. Sevilla, S. Ellis, The far ultra-violet imager on the ICON mission. *Space Sci. Rev.* (2017). <https://doi.org/10.1007/s11214-017-0386-0>
- W. Menke, *Geophysical Data Analysis: Discrete Inverse Theory*. Int. Geophys. Ser., vol. 45 (Academic Press, San Diego, 1989). 289 pp.
- L.J. Paxton et al., SSUSI: horizon-to- horizon and limb viewing spectrographic imager for remote sensing of environmental parameters, in *Proc. SPIE 1764, Ultraviolet Technology IV* (1992). <https://doi.org/10.1117/12.140846>
- J.M. Picone, A.E. Hedin, D.P. Drob, A.C. Aikin, NRLMSISE00 empirical model of the atmosphere: statistical comparisons and scientific issues. *J. Geophys. Res.* **107**(A12), 1468 (2002). <https://doi.org/10.1029/2002JA009430>
- P.G. Richards, R.R. Meier, P.J. Wilkinson, On the consistency of satellite measurements of thermospheric composition and solar EUV irradiance with Australian ionosonde electron density data. *J. Geophys. Res.* **115**, A10309 (2010). <https://doi.org/10.1029/2010JA015368>
- M.M. Sirk et al., Design and performance of the ICON EUV spectrograph. *Space Sci. Rev.* (2017). <https://doi.org/10.1007/s11214-017-0384-2>

- A.W. Stephan, E.J. Korpela, M.M. Sirk, S.L. England, T.J. Immel, Daytime ionosphere retrieval algorithm for the Ionospheric Connection Explorer (ICON). *Space Sci. Rev.* (2017). <https://doi.org/10.1007/s11214-017-0385-1>
- A.W. Stephan, R.R. Meier, L.J. Paxton, Comparison of Global Ultraviolet Imager limb and disk observations of column O/N₂ during a geomagnetic storm. *J. Geophys. Res.* **113**, A01301 (2008). <https://doi.org/10.1029/2007JA012599>
- D.J. Strickland et al., Atmospheric Ultraviolet Radiance Integrated Code (AURIC): theory, software architecture, inputs, and selected results. *J. Quant. Spectrosc. Radiat. Transf.* **62**, 689–742 (1999). [https://doi.org/10.1016/S0022-4073\(98\)00098-3](https://doi.org/10.1016/S0022-4073(98)00098-3)
- D.J. Strickland, J.D. Craven, R.E. Daniell Jr., Six days of thermospheric-ionospheric weather over the Northern Hemisphere in late September 1981. *J. Geophys. Res.* **106**(A12), 30291–30306 (2001). <https://doi.org/10.1029/2001JA001113>
- D.J. Strickland, J.S. Evans, L.J. Paxton, Satellite remote sensing of thermospheric O/N₂ and solar EUV: 1. Theory. *J. Geophys. Res.* **100**(A7), 12217–12226 (1995). <https://doi.org/10.1029/95JA00574>
- D.J. Strickland, J.S. Evans, J. Correia, Comment on “Long-term variation in the thermosphere: TIMED/GUVI observations” by Y. Zhang and L.J. Paxton. *J. Geophys. Res.* **117**, A07302 (2012). <https://doi.org/10.1029/2011JA017350>
- T.N. Woods et al., XUV Photometer System (XPS): improved solar irradiance algorithm using CHIANTI spectral models. *Sol. Phys.* **250**, 235–267 (2008). <https://doi.org/10.1007/s11207-008-9196-6>
- Y. Zhang, L.J. Paxton, Reply to comment by D.J. Strickland et al. on “Long-term variation in the thermosphere: TIMED/GUVI observations”. *J. Geophys. Res.* **117**, A07304 (2012). <https://doi.org/10.1029/2012JA017594>
- Y. Zhang, L.J. Paxton, D. Morrison, B. Wolven, H. Kil, C.-I. Meng, S.B. Mende, T.J. Immel, O/N₂ changes during 1–4 October 2002 storms: IMAGE SI-13 and TIMED/GUVI observations. *J. Geophys. Res.* **109**, A10308 (2004). <https://doi.org/10.1029/2004JA010441>